THE JOURNAL OF PHYSICAL CHEMISTRY C

pubs.acs.org/JPCC Article

Quantitative Specifications to Avoid Degradation during E-Beam and Induced Current Microscopy of Halide Perovskite Devices

Yanqi Luo, Pritesh Parikh, Thomas M. Brenner,* Min-cheol Kim, Rui Wang, Yang Yang, Juan-Pablo Correa-Baena, Tonio Buonassisi, Ying Shirley Meng, and David P. Fenning*

Cite This: https://dx.doi.org/10.1021/acs.jpcc.0c06733 Read Online

ACCESS | Metrics & More | Article Recommendations | Supporting Information

ABSTRACT: Degradation due to electron beam exposure has posed a challenge in the use of electron microscopy to probe halide perovskite materials and devices. In this study, the interaction between the electron beam and the perovskite across acceleration voltages and at low probe currents is investigated in a scanning electron microscope (SEM) by monitoring the electron-beam-induced current (EBIC) response in perovskite solar cells in a plan-view configuration. SEM probe conditions are identified where dozens of repeated scans over a single region of the perovskite solar cell induce minimal electronic degradation. Overall, the induced current response of the perovskite device is found to strongly depend upon the beam condition: rapid decay occurs at high beam powers, the current activates at the lowest beam powers, and a newfound quasi-steady response is revealed at intermediate beam conditions. A quantitative window for the successful conduction of e-beam studies with minimal electronic degradation is revealed by evaluating induced current response over a wide range of perovskite devices, which invites broader use of SEM-based characterization techniques, including EBIC, as powerful techniques for correlative microscopy investigations.

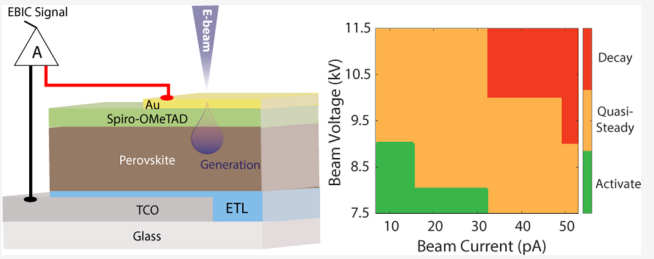

INTRODUCTION

Hybrid perovskites have attracted significant attention in recent years, particularly in optoelectronic applications.[1−3] Electron-beam (e-beam) microscopy has traditionally been a valuable multimodal characterization platform to assess micro- and nanoscale variations in chemistry, structure, morphology, and electronic properties of thin-film materials.[4−6] Due to the presence of nanoscopic variation in halide perovskites,[7] microscopy techniques can help build a more comprehensive understanding of the origins of material degradation mechanisms in perovskites as well as identify opportunities to further reduce carrier recombination in operating devices.

However, unlike conventional semiconductors, hybrid perovskites are challenging to characterize due to their instability under many probes, including electron beams and intense irradiation.[8] The formation of intermediate or degraded phases was evidenced in transmission electron microscopy (TEM) by the appearance of forbidden reflections in methylammonium lead iodide ($MAPbI_3$, MA = $CH_3NH_3^+$) after 1 min of continuous e-beam irradiation at 200 kV and 2 e-Å^{-2} s^{-1}.[9] Methylammonium lead bromide ($MAPbBr_3$) has similarly been reported to lose crystallinity under an accumulated dose of 10−20 e-Å^{-2} at an e-beam voltage of 300 kV during high-resolution TEM (HRTEM) measurements.[10] Reducing required dose by ∼6000× relative to a traditional sulfur detector[11] and leveraging the capabilities of new high-sensitivity detectors, Adhyaksa et al. demonstrated successful scanning electron microscope (SEM)-based electron backscattered diffraction (EBSD) mapping to elucidate the grain boundary characteristics in $MAPbBr_3$ thin film using 100 pA with 0.1 s dwell time per pixel at 30 kV.[6] Jariwala et al. revealed the impact of crystal misorientation on nonradiative recombination in $MAPbI_3$ thin film by EBSD mapping with a much lower beam voltage of 6 kV.[12] Given the signal-starved nature of scattering experiments, structural characterization of perovskite materials using e-beam microscopies has often meant pushing the limit of detector capabilities and/or carefully tuning beam conditions.

E-beam based methods can also examine optoelectronic performance at the nanoscale, with the advantage that such methods benefit from signal amplification due to the incident electron interaction with the sample. Through a cascade of inelastic scattering, the high-energy incident electrons generate a multitude of charge carriers that thermalize to the semiconductor band edges. The electron-beam analogs of photoluminescence (PL) and laser-beam-induced current (LBIC), cathodoluminescence (CL), and electron-beam-

Received: July 22, 2020
Published: August 3, 2020

induced current (EBIC) can monitor the recombination or extraction of these charges. Xiao et al. assessed beam-induced degradation in iodine-containing perovskites,[13] where the samples exhibited CL peak broadening and a new blue-shifted CL peak with increasing beam power and dose. CL can yield local optoelectronic insights when avoiding beam-induced degradation. Hentz et al. found that local iodide segregation intensified band-to-band CL at iodide-rich aggregates identified by dark-field scanning transmission electron microscopy (STEM).[14]

In contrast to CL on films, e-beam-induced current (EBIC) is used on devices to identify heterogeneous recombination activity and charge carrier collection due to composition variations, structural defects, or impurities.[4,15−17] It can also provide valuable insights into understanding device operating mechanisms by identifying the location of charge-separating junctions in cross-section and enabling quantitative measurement of carrier diffusion lengths to those junctions.[18,19] Cross-sectional EBIC performed by Edri et al. confirmed the p−i−n operating mechanism in $MAPbI_{3-x}Cl_x$ perovskites,[20] whereas $MAPbBr_3$ cells were identified to operate as p−n junction type cells by Kedem et al.[21,22] Plan-view EBIC can help demystify the role of chemical composition or structure defects on carrier generation and collection. For example, recently Rb-rich aggregates were found to be photoinactive and weakly recombination-active by plan-view EBIC in Rb-containing quaternary A-site perovskites.[23] Besides the investigation of carrier collection heterogeneities, plan-view EBIC can also be used to extract carrier diffusion length for both holes and electrons by capturing the carrier diffusion profile onto selective contacts, as recently quantified for mixed halide perovskites.[24] Because EBIC is affected by the collection efficiency of band edge carriers, minority carrier devices that have better collection efficiency and thus better overall performance should, in principle, yield higher EBIC signal than poorly performing devices. EBIC has been used accordingly to detect and evaluate variations in device performance, as has been demonstrated for traditional semiconductors.[25,26]

Despite these pioneering studies, compared to traditional semiconducting materials,[4,16,27,28] perovskite solar cells have seen relatively little application to date of EBIC or correlative microscopy studies on devices incorporating e-beam characterization with other *ex situ* characterization on the same areas because of the unique challenges presented by this class of materials, namely poor beam stability and related dose- and rate-dependent activation and decay effects. In this study, we identify an experimental window where little e-beam-induced degradation is seen in perovskite solar cells, as evidenced by the relative stability of the dose-dependent EBIC current, which is sensitive to electronic defect concentration. Monte Carlo electron trajectory simulations (using CASINO[29]) quantify the findings in terms of energy deposited in the perovskite layer, so that the results can be generalized to perovskite devices of even very different architectures and for other e-beam-based characterization methods such as SEM or CL.

EXPERIMENTAL SECTION

Exploring devices with varying composition, architecture, and methods of absorber deposition is required to provide a generalized operating window for performing EBIC analysis on halide perovskite devices. Figure 1 details the perovskite

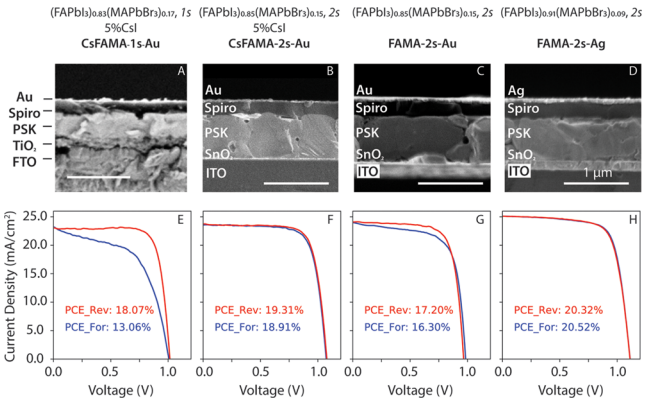

Figure 1. Composition, device architecture, and device performance of samples studied using EBIC. The cross-sectional SEM images and the 1-sun current−voltage (J−V) measurements of each device are shown in (A−D) and (E−H), respectively.

devices that were investigated, including the expected absorber compositions, the methods of fabrication, device architectures, and device performance. The selected absorber compositions and device architectures were developed recently in the literature. The addition of $MAPbBr_3$ to $FAPbI_3$ (FA = $CH(NH_2)_2^+$, formamidinium) in small quantities has been demonstrated to produce high-performing devices.[30,31] Incorporating a small fraction of CsI in the mixed A-site and halide perovskites has been widely adopted to fabricate devices with repeatability, stability, and performance.[32,33] As shown in Figure 1, the nominal absorber compositions are grouped into two different categories, ones with CsI addition and ones without. In addition, the selected devices have differences in the deposition method of the absorber (i.e., one-step (1s) vs two-step (2s)). All devices have Spiro-OMeTAD as the hole transport layer (HTL) and mesoporous TiO_2 (m-TiO_2) or SnO_2 as the electron transport layer (ETL), where m-TiO_2 has been shown to enhance the adhesion between perovskite and ETL,[34,35] and planar SnO_2 reduces the interface complexity[36] and provides better band edge alignment with perovskite layer.[37] Device fabrication detail is provided in the Supporting Information. In this work, samples are denoted using A-site composition followed by the deposition method and metal back contact. The cross-sectional SEM images and the 1-sun current−voltage (J−V) measurements of each device are shown in Figure 1A−D and E−H, respectively.

The configuration for plan-view EBIC is shown in Figure 2A, where the beam interacts with the absorber by penetrating through the backside Au contact and the hole transport layer (HTL, Spiro-OMeTAD). As shown in the schematic, when the device is contacted externally, excited carriers can be collected as electron-beam-induced current. We connect the device in short-circuit conditions to a preamplifier (Femto DLPCA-200) whose output is synchronized with the microscope scan generator using a Mighty EBIC 2.0 controller (Ephemeron Labs). The plan-view configuration has a major advantage over cross-sectional EBIC for this study: finer control over power deposited in the perovskite because of the overlying top contact.

Monte Carlo electron trajectory simulations using CASINO[38−40] were used to identify the range of acceleration voltages for which the electron beam probe reaches the perovskite beneath the overlying layers in the solar cell. Cross-sectional SEM images of the cells are shown in Figure 1A−D,

https://dx.doi.org/10.1021/acs.jpcc.0c06733
J. Phys. Chem. C XXXX, XXX, XXX−XXX

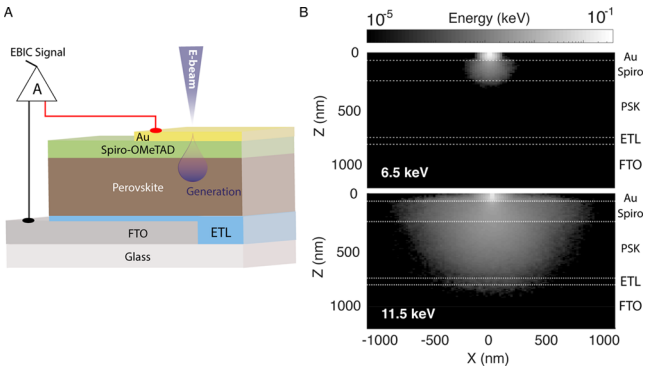

Figure 2. (A) Experimental setup of plan-view EBIC measurement. A beam voltage is chosen such that the e-beam penetrates sufficiently through the backside Au contact and excites carriers within the perovskite bulk. The charge carriers are collected via the selective contact layers, and this EBIC current amplified externally for detection. (B) Simulation of energy deposited in the device layers per incident electron at a beam voltage of 6.5 (top) and 11.5 kV (bottom), in which the Au, Spiro, and perovskite (PSK) are 70, 180, and 500 nm thick, respectively.

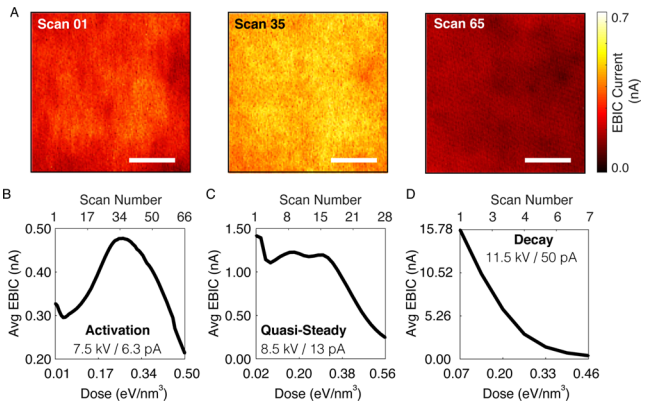

Figure 3. (A) Selected scans from a time series of plan-view EBIC maps showing the activation response of the 5% CsI + $(FAPbI_3)_{0.83}(MAPbBr_3)_{0.17}$ device under 7.5 kV/6.3 pA. Scale bar: 10 μm. (B–D) Three characteristic EBIC profiles showing activation, quasi-steady, and decay responses, obtained by plotting the average EBIC signal collected from the EBIC maps as a function of accumulated energy dose in the perovskite.

from which layer thicknesses were extracted to construct an accurate device model for CASINO simulation provided in Table S1. CASINO estimates the scattering, trajectory, and differential energy loss of electrons interacting with a given material from the probabilities of electron–matter interactions.[38] From the simulations, an operating window from 6.5 to 11.5 kV was established using Au and HTL thickness of 70 and 180 nm, respectively. The simulated interactions at 6.5 and 11.5 kV are shown in cross-section in Figure 2B, in which whiter pixels have higher energy deposited. The penetration depth is shallow at 6.5 keV, and the interaction volume just passes the HTL/perovskite interface. Conversely, a large interaction volume appears at 11.5 keV, extending just into the FTO. Thus, by examining accelerating voltages from 6.5 to 11.5 kV we can generate EBIC and extend the probe through the perovskite thickness. Selecting beam currents near the lower limit of widely accessible SEMs, an experimental matrix of beam voltages (within a range of 6.5–11.5 kV) and nominal beam currents between 6.3 and 50 pA (measured beam currents reported in Table S2 differ by <20%) were identified for investigation. The EBIC investigation was performed in a sequence of increasing beam power and stopped once exponential signal decay was observed. A dwell time per point of 26.5 μs was used throughout, and previously unexposed nearby regions tested for each new beam condition.

RESULTS AND DISCUSSION

We find an activation of the beam-induced current at the lowest e-beam powers, similar to two previous reports[8,24] for the CsFAMA-1s-Au perovskite. In Figure 3A, three EBIC maps selected from a set of repeated scans of the same area carried out at 7.5 kV and 6.3 pA are shown (scans 1, 35, and 65). Under these conditions, the perovskite device starts with relatively low area-averaged EBIC current of 0.33 ± 0.06 nA. A brief initial decay is always present, but over successive scanning, the map brightens, until after 35 scans the highest EBIC signal is observed with an average of 0.48 ± 0.06 nA. The EBIC signal then gradually decays upon further scanning, as seen in the 65th scan. Similar optoelectronic activation is observed in the visible light–perovskite interaction as well, such as PL enhancement after light soaking.[41,42] The presence of an activation response suggests one of the following (1) the stabilization or filling of traps by the excited carriers or the incident electrons from the beam,[8,43] (2) lead halide formation and surface passivation after e-beam interaction,[44,45] and/or (3) thermal annealing of the absorber by the beam.

Under higher beam powers, we observe two distinct EBIC responses: at intermediate power, we find a "quasi-steady" response before decay finally sets in, and finally at "high" power, a direct decay of permanent degradation. The quasi-steady response is defined semiquantitatively as occurring when multiple local maxima are present in the derivative of the EBIC signal with respect to absorbed dose (shown in Figure S1), which suggests more than one dose-dependent process is occurring. Examples of the three EBIC responses observed are shown in Figure 3B–D, where the average EBIC from successive maps is shown as a function of scan number (top axis) and energy dose absorbed in the perovskite normalized by the beam interaction volume in the perovskite layer (eV/nm^3) as calculated by CASINO simulation (bottom axis). This dose represents the volumetric energy density deposited in the perovskite and is used to examine dose effects as an intensive quantity (see the Supporting Information and Figure S2 for details on interaction volume simulations). In Figure 3B, the activation response from the same area shown in Figure 3A is displayed, where the maximum EBIC current is collected during the 35th scan, equivalent to an absorbed dose of 0.27 eV/nm^3. When the beam power is slightly higher, 8.5 kV/13 pA, a quasi-steady response is observed after a brief initial decay where the EBIC current remains almost unchanged from scan 8 to 15 as seen in Figure 3C (a dose range of 0.16–0.30 eV/nm^3). On the other hand, the highest beam power (11.5 kV/50 pA) tested results in an almost 30% reduction of EBIC signal after the third scan (Figure 3D).

The type of EBIC response observed does not appear to be strongly influenced by the total accumulated energy dose (as shown in Figure 3), but it is strongly related to the *power* absorbed in the perovskite. A categorization of the EBIC response—activation, quasi-steady, or decay—as a function of beam current and beam voltage is provided in Figure 4, with contours indicating lines of constant power absorbed in the

https://dx.doi.org/10.1021/acs.jpcc.0c06733
J. Phys. Chem. C XXXX, XXX, XXX–XXX

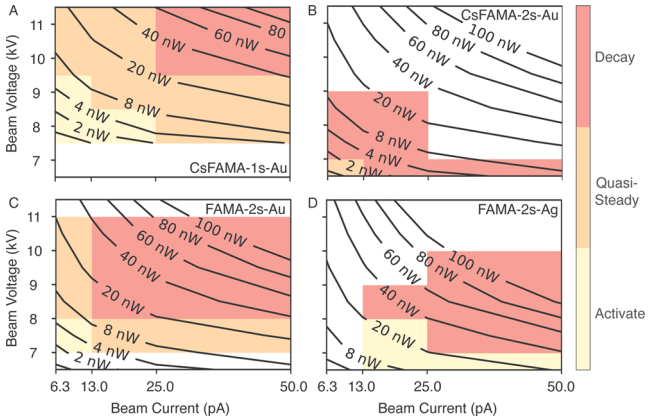

Figure 4. Categorical heat map of EBIC responses for beam current and voltage combinations of all four perovskite devices: yellow for "activation," orange for "quasi-steady," and red for "decay." The contour lines are lines of constant absorbed power in the perovskite with a unit of nW per point.

perovskite, accounting for the thickness differences in the overlying Au/Ag and Spiro-OMeTAD layer, calculated in CASINO (nW per point per scan). The EBIC response at every beam condition and its categorization are shown in Figure S1. Given that current varies by a factor of 5 but voltage by less than a factor of 2 across this parameter space, the characteristic EBIC response is evidently more sensitive to the e-beam voltage than the incident beam current. However, the type of EBIC response most closely follows the contours of power absorbed in the perovskite.

The changing EBIC response as a function of absorbed beam power is most evident in Figure 4A. In this particular system, the CsFAMA-1s-Au device, an activation response is seen when the power absorbed in the perovskite per point is less than 4 nW, decay EBIC profiles are mainly observed at beam powers above 20 nW, and quasi-steady responses can be found from 6 to 20 nW. Notably, activation and decay responses in literature reports of cross-sectional EBIC[8,20] also appear to follow these bounds (as shown in Figure S3)—activation is seen when <6 nW is absorbed in the perovskite per point and decay is seen when >40 nW is absorbed per point. This correspondence between cross-sectional experiments, where the perovskite is directly exposed to the beam, and the plan-view experiments here, despite the overlying HTL and Au layers but with beam conditions chosen to deliver electrons to the perovskite (as would also be the case for SEM energy-dispersive X-ray spectroscopy (EDS) or other analytical microscopies), suggests that the type of EBIC response is mainly a result of the beam−perovskite interaction.

The relationship between absorbed power and the EBIC response is monotonic across the spectrum of devices and compositions tested here—but the finer variations between the devices indicate variability in E-beam stability dependent on the fabrication method, absorber composition, and device architecture. Most notably, the E-beam stability does not directly correlate with the device efficiency. As compared with devices fabricated using 1s, samples prepared using 2s are more sensitive to E-beam exposure since the decay response appears at lower beam power for samples having the same Au metal contact (i.e., CsFAMA-1s-Au, CsFAMA-2s-Au, and FAMA-2s-Au). Because the HTL is also the same (Spiro-OMeTAD), the shift of the decay toward smaller beam power suggests that 2s absorbers are more e-beam sensitive. This beam sensitivity results in a narrowing of the window where quasi-steady is seen (Figure 4B−D).

Composition dependence cannot be neglected, as composition engineering has been shown to be an effective approach to improve absorber stability.[46,47] We speculate that device stability under e-beam may be associated with the Br concentration in the absorbers, where increasing stability is seen here as Br fraction increases. This observation is in general agreement with literature findings of 1-sun stability, in which devices that have over 1000 h stability under continuous illumination are composed of Br substituent with $x > 0.11$ in $APb(I_{1-x}Br_x)_3$, mixed A-site and halide system.[33,48,49] Higher Br content introduces several underlying changes that may affect beam stability including improved formability and/or a higher cohesive energy.[50,51] Although disentangling stability contributions from changes in composition as compared with the concomitant small changes in fabrication recipe is difficult, 7 kV/6.3 pA can be considered as a starting beam voltage and current combination for characterizing perovskites with Spiro-OMeTAD (or similar organic HTL, ∼180 nm thickness) and a thin (∼70 nm) metallic back contact. The beam voltage may be need to be tuned up (down) modestly depending upon the presence of a thicker (thinner) HTL or back contact to achieve a high-quality EBIC signal while avoiding unnecessary damage.

The EBIC data provide evidence that at least two distinct dose-dependent processes occur in the perovskite device during e-beam interaction. These processes are highly sensitive to the beam power reaching the perovskite, causing qualitative changes to the dose response including the dominance of degradation processes at high power. The sensitivity to beam power may indicate that the rate of these processes depends on (1) the energy of the electrons incident on the perovskite layer, such as knock-on effects in the inelastic scattering process, and/or that it depends on (2) the power density, such as in local heating (which has previously been discussed).[8] The quasi-steady response appears to be the superposition (or possibly interaction) of multiple photophysical processes occurring simultaneously. It perhaps indicates the competition between degradation and carrier-induced brightening, or a self-repairing mechanism involving lattice expansion or lattice reordering.[42] In less stable devices, the narrower window of the quasi-steady response suggests degradation dominates over other photophysical processes. As a result, a finer interval of beam power is needed to capture the quasi-steady response while establishing the optimal dose window. In general, the quasi-steady window can provide an extended range of experimental conditions where EBIC or other electron microscopy can be conducted successfully without immediate degradation.

Having clearly defined experimental conditions for successful E-beam characterization enables EBIC as part of a suite of tools for understanding the interplay of device-limiting defects in halide perovskites. With quantification of the probe-related degradation established, correlative microscopy such as with sub-band optical spectroscopy can pursue a deeper understanding of the defects involved. However, some care must be taken in transferring the success of the operating beam current and voltage conditions reported here to other microscopes and samples. In particular, the necessary voltages for the interaction volume to reach the absorber will be architecture-dependent. Evaluating the experimentally desirable accelerating voltage and current for a particular device architecture and measure-

https://dx.doi.org/10.1021/acs.jpcc.0c06733
J. Phys. Chem. C XXXX, XXX, XXX−XXX

ment configuration using CASINO is encouraged prior to executing EBIC. We provide a user executable package for processing CASINO output files to help transfer this result to different perovskite solar cell architectures.[52] We note that because the perovskite is more sensitive to electron acceleration voltage, it may be favorable to increase beam current to achieve sufficient EBIC signal-to-noise if necessary. With typical layer thickness of Au (70 nm) and HTL (180 nm), we recommend starting plan-view EBIC measurement at 7 kV/6.3 pA to avoid rapid beam damage on the samples.

CONCLUSIONS

Plan-view EBIC can be seen as a promising—and even reliable—perovskite characterization approach to probe nanoscale current collection in operational perovskite devices, identify defects, and assess device quality and/or stability. Potential applications include exploring the underlying role of composition variations and passivants such as in quasi-2D perovskites[53,54] or additives such as thiocyanate[55] and to provide feedback for perovskite manufacturing scaling efforts, as is common in traditional semiconductor technology. Using the experimental windows provided here, SEM-based characterization can be carried out with confidence.

ASSOCIATED CONTENT

Supporting Information

The Supporting Information is available free of charge at https://pubs.acs.org/doi/10.1021/acs.jpcc.0c06733.

Device fabrication details; summary of layer thicknesses of all devices studied (Table S1); detailed EBIC experimental description; CASINO simulation details; EBIC response as a function of acceleration voltage and beam current (Figure S1); calculated interaction volume as a function of beam voltage (Figure S2); calculated absorbed power in the perovskite per point in cross-section EBIC (Figure S3); beam current measurements by Faraday cup (Table S2) (PDF)

AUTHOR INFORMATION

Corresponding Authors

Thomas M. Brenner − *Department of Nanoengineering, University of California San Diego, La Jolla, California 92093, United States;* orcid.org/0000-0002-1135-6112; Email: tomas-michael.brenner@weizmann.ac.il

David P. Fenning − *Department of Nanoengineering and Chemical Engineering Program, University of California San Diego, La Jolla, California 92093, United States;* orcid.org/0000-0002-4609-9312; Email: dfenning@eng.ucsd.edu

Authors

Yanqi Luo − *Department of Nanoengineering, University of California San Diego, La Jolla, California 92093, United States;* orcid.org/0000-0001-5624-9583

Pritesh Parikh − *Department of Nanoengineering, University of California San Diego, La Jolla, California 92093, United States;* orcid.org/0000-0003-2258-5719

Min-cheol Kim − *Department of Nanoengineering, University of California San Diego, La Jolla, California 92093, United States*

Rui Wang − *Department of Materials Science and Engineering and California NanoSystems Institute, University of California, Los Angeles, California 90095, United States;* orcid.org/0000-0003-2185-0752

Yang Yang − *Department of Materials Science and Engineering and California NanoSystems Institute, University of California, Los Angeles, California 90095, United States;* orcid.org/0000-0001-8833-7641

Juan-Pablo Correa-Baena − *Massachusetts Institute of Technology, Cambridge, Massachusetts 02139, United States;* orcid.org/0000-0002-3860-1149

Tonio Buonassisi − *Massachusetts Institute of Technology, Cambridge, Massachusetts 02139, United States*

Ying Shirley Meng − *Department of Nanoengineering, University of California San Diego, La Jolla, California 92093, United States;* orcid.org/0000-0001-8936-8845

Complete contact information is available at: https://pubs.acs.org/10.1021/acs.jpcc.0c06733

Notes

The authors declare no competing financial interest.

ACKNOWLEDGMENTS

Y.L., P.P., Y.S.M., and D.P.F. are grateful for the financial support of a California Energy Commission Advance Breakthrough award (EPC-16-050). J.-P.C.-B. acknowledges the support of a Department of Energy (DOE) EERE Postdoctoral Research Award. R.W. and Y.Y. acknowledge the support of the U.S. Department of Energy's Office of Energy Efficiency and Renewable Energy (EERE) under the Solar Energy Technologies Office Award Number DE-EE0008751. This EBIC work was performed in part at the San Diego Nanotechnology Infrastructure (SDNI) of UCSD, a member of the National Nanotechnology Coordinated Infrastructure, which is supported by the National Science Foundation (Grant ECCS-1542148).

REFERENCES

(1) National Renewable Energy Laboratory (NREL). Best Research-Cell Efficiencies. https://www.nrel.gov/pv/assets/images/efficiency-chart.png; 2020.

(2) Wei, H.; Fang, Y.; Mulligan, P.; Chuirazzi, W.; Fang, H.-H.; Wang, C.; Ecker, B. R.; Gao, Y.; Loi, M. A.; Cao, L.; et al. Sensitive X-Ray Detectors Made of Methylammonium Lead Tribromide Perovskite Single Crystals. *Nat. Photonics* **2016**, *10*, 333−339.

(3) Zhang, X.; Liu, H.; Wang, W.; Zhang, J.; Xu, B.; Karen, K. L.; Zheng, Y.; Liu, S.; Chen, S.; Wang, K.; et al. Hybrid Perovskite Light-Emitting Diodes Based on Perovskite Nanocrystals with Organic-Inorganic Mixed Cations. *Adv. Mater.* **2017**, *29*, No. 1606405.

(4) Chang, C.-C.; Chi, C.-Y.; Yao, M.; Huang, N.; Chen, C.-C.; Theiss, J.; Bushmaker, A. W.; Lalumondiere, S.; Yeh, T.-W.; Povinelli, M. L.; et al. Electrical and Optical Characterization of Surface Passivation in GaAs Nanowires. *Nano Lett.* **2012**, *12*, 4484−4489.

(5) Wilkinson, A. J.; Britton, T. B. Strains, Planes, and EBSD Electron Back Scatter Diffraction (EBSD) Has Made an Impressive Impact. *Mater. Today* **2012**, *15*, 366−376.

(6) Adhyaksa, G. W. P.; Brittman, S.; Haralds, A.; Lof, A.; Li, X.; Keelor, J. D.; Luo, Y.; Duevski, T.; Heeren, R. M. A.; Ellis, S. R.; et al. Understanding Detrimental and Beneficial Grain Boundary Effects in Halide Perovskites. *Adv. Mater.* **2018**, *30*, No. 1804792.

(7) Tennyson, E. M.; Doherty, T. A. S.; Stranks, S. D. Heterogeneity at Multiple Length Scales in Halide Perovskite Semiconductors. *Nat. Rev. Mater.* **2019**, *4*, 573−587.

(8) Klein-Kedem, N.; Cahen, D.; Hodes, G. Effects of Light and Electron Beam Irradiation on Halide Perovskites and Their Solar Cells. *Acc. Chem. Res.* **2016**, *49*, 347−354.

(9) Rothmann, M. U.; Li, W.; Zhu, Y.; Liu, A.; Ku, Z.; Bach, U.; Etheridge, J.; Cheng, Y. Structural and Chemical Changes to

$CH_3NH_3PbI_3$ Induced by Electron and Gallium Ion Beams. *Adv. Mater.* **2018**, *30*, No. 1800629.
(10) Zhang, D.; Zhu, Y.; Ying, X.; Hsiung, C.; Sougrat, R.; Li, K.; Han, Y.; et al. Atomic-Resolution Transmission Electron Microscopy of Electron Beam—Sensitive Crystalline Materials. *Science* **2018**, *359*, 675−679.
(11) Khoram, P.; Brittman, S.; Dzik, W. I.; Reek, J. N. H.; Garnett, E. C. Growth and Characterization of PDMS-Stamped Halide Perovskite Single Microcrystals. *J. Phys. Chem. C* **2016**, *120*, 6475−6481.
(12) Jariwala, S.; Sun, H.; Adhyaksa, G. W. P.; Lof, A.; Garnett, E. C.; Ginger, D. S.; et al. Imaging Grain Structure in Halide Perovskites: Local Crystal Misorientation Influences Non-Radiative Recombination. *Joule* **2019**, *3*, 3048−3060.
(13) Xiao, C.; Li, Z.; Guthrey, H.; Moseley, J.; Yang, Y.; Wozny, S.; Moutinho, H.; To, B.; Berry, J. J.; Gorman, B.; et al. Mechanisms of Electron-Beam-Induced Damage in Perovskite Thin Films Revealed by Cathodoluminescence Spectroscopy. *J. Phys. Chem. C* **2015**, *119*, 26904−26911.
(14) Hentz, O.; Zhao, Z.; Gradecak, S. Impacts of Ion Segregation on Local Optical Properties in Mixed Halide Perovskite Films. *Nano Lett.* **2016**, *16*, 1485−1490.
(15) Kveder, V.; Kittler, M.; Schröter, W. Recombination Activity of Contaminated Dislocations in Silicon: A Model Describing Electron-Beam-Induced Current Contrast Behavior. *Phys. Rev. B* **2001**, *63*, No. 115208.
(16) Wang, Z. J.; Tsurekawa, S.; Ikeda, K.; Sekiguchi, T.; Watanabe, T. Relationship between Electrical Activity and Grain Boundary Structural Configuration in Polycrystalline Silicon. *Interface Sci.* **1999**, *7*, 197−205.
(17) Orlov, V. I.; Feklisova, O. V.; Yakimov, E. B. A Comparison of EBIC, LBIC and XBIC Methods as Tools for Multicrystalline Si Characterization. *Solid State Phenom.* **2014**, *205*−*206*, 142−147.
(18) Leamy, H. J. Charge Collection Scanning Electron Microscopy. *J. Appl. Phys.* **1982**, *53*, R51−R80.
(19) Matson, R. J.; Noufi, R.; Ahrenkiel, R. K.; Powell, R. C.; Cahen, D. EBIC Investigations of Junction Activity and the Role of Oxygen in $CdS/CuInSe_2$ Devices. *Sol. Cells* **1986**, *16*, 495−519.
(20) Edri, E.; Kirmayer, S.; Mukhopadhyay, S.; Gartsman, K.; Hodes, G.; Cahen, D. Elucidating the Charge Carrier Separation and Working Mechanism of $CH_3NH_3PbI_{3-x}Cl_x$ Perovskite Solar Cells. *Nat. Commun.* **2014**, *5*, No. 3461.
(21) Kedem, N.; Brenner, T. M.; Kulbak, M.; Schaefer, N.; Levcenko, S.; Levine, I.; Abou-Ras, D.; Hodes, G.; Cahen, D. Light-Induced Increase of Electron Diffusion Length in a p-n Junction Type $CH_3NH_3PbBr_3$ Perovskite Solar Cell. *J. Phys. Chem. Lett.* **2015**, *6*, 2469−2476.
(22) Kedem, N.; Kulbak, M.; Brenner, T. M.; Hodes, G.; Cahen, D. Type-Inversion as a Working Mechanism of High Voltage $MAPbBr_3(Cl)$-Based Halide Perovskite Solar Cells. *Phys. Chem. Chem. Phys.* **2017**, *19*, 5753−5762.
(23) Correa-Baena, J.-P.; Luo, Y.; Brenner, T. M.; Snaider, J.; Sun, S.; Li, X.; Jensen, M. A.; Titan, N.; Hartono, P.; Nienhaus, L.; et al. Homogenized Halides and Alkali Cation Segregation in Alloyed Organic-Inorganic Perovskites. *Science* **2019**, *363*, 627−631.
(24) Park, B.; Kedem, N.; Kulbak, M.; Lee, D. Y.; Yang, W. S.; Jeon, N. J.; Seo, J.; Kim, G.; Kim, K. J.; Shin, T. J.; et al. Understanding How Excess Lead Iodide Precursor Improves Halide Perovskite Solar Cell Performance. *Nat. Commun.* **2018**, *9*, No. 3301.
(25) Kurniawan, O.; Ong, V. K. S. Determination of Diffusion Lengths with the Use of EBIC from a Diffused Junction with Any Values of Junction Depths. *IEEE Trans. Electron Devices* **2006**, *53*, 2358−2363.
(26) Fell, T. S.; Wilshaw, P. R.; De Coteau, M. D. EBIC Investigations of Dislocations and Their Interactions with Impurities in Silicon. *Phys. Status Solidi A* **1993**, *138*, 695−704.
(27) Hieslmair, H.; Istratov, A. A.; Sachdeva, R.; Weber, E. *New Synchrotron-Radiation Based Technique to Study Localized Defects in Silicon: "EBIC" with X-Ray Excitation*, Crystalline Silicon Solar Cell Materials and Processes; 2000; Vol. *33*, pp 162−165.
(28) Kittler, M.; Seifert, W. On the Origin of EBIC Defect Contrast in Silicon. A Reflection on Injection and Temperature Dependent Investigations. *Phys. Status Solidi A* **1993**, *138*, 687−693.
(29) Demers, H.; Poirier-Demers, N.; Couture, A. R.; Joly, D.; Guilmain, M.; De Jonge, N.; Drouin, D. Three-Dimensional Electron Microscopy Simulation with the CASINO Monte Carlo Software. *Scanning* **2011**, *33*, 135−146.
(30) Jung, E. H.; Jeon, N. J.; Park, E. Y.; Moon, C. S.; Shin, T. J.; Yang, T.-Y.; Noh, J. H.; Seo, J. Efficient, Stable and Scalable Perovskite Solar Cells Using Poly(3-Hexylthiophene). *Nature* **2019**, *567*, 511−515.
(31) Wang, R.; Xue, J.; Wang, K. L.; Wang, Z. K.; Luo, Y.; Fenning, D.; Xu, G.; Nuryyeva, S.; Huang, T.; Zhao, Y.; et al. Constructive Molecular Configurations for Surface-Defect Passivation of Perovskite Photovoltaics. *Science* **2019**, *366*, 1509−1513.
(32) Bai, S.; Da, P.; Li, C.; Wang, Z.; Yuan, Z.; Fu, F.; Kawecki, M.; Liu, X.; Sakai, N.; Wang, J. T. W.; et al. Planar Perovskite Solar Cells with Long-Term Stability Using Ionic Liquid Additives. *Nature* **2019**, *571*, 245−250.
(33) Xu, J.; Boyd, C. C.; Yu, Z. J.; Palmstrom, A. F.; Witter, D. J.; Larson, B. W.; France, R. M.; Werner, J.; Harvey, S. P.; Wolf, E. J.; et al. Triple-Halide Wide−Band Gap Perovskites with Suppressed Phase Segregation for Efficient Tandems. *Science* **2020**, *367*, 1097−1104.
(34) Bi, D.; Tress, W.; Dar, M. I.; Gao, P.; Luo, J.; Renevier, C.; Schenk, K.; Abate, A.; Fabrizio, G.; Baena, J. C.; et al. Efficient Luminescent Solar Cells Based on Tailored Mixed-Cation Perovskites Efficient Luminescent Solar Cells Based on Tailored Mixed-Cation Perovskites. *Sci. Adv.* **2016**, *2*, No. e1501170.
(35) Saliba, M.; Matsui, T.; Domanski, K.; Seo, J.-Y.; Ummadisingu, A.; Zakeeruddin, S. M.; Correa-Baena, J.-P.; Tress, W. R.; Abate, A.; Hagfeldt, A.; et al. Incorporation of Rubidium Cations into Perovskite Solar Cells Improves Photovoltaic Performance. *Science* **2016**, *354*, 206−209.
(36) Zhao, Y.; Nardes, A.; Zhu, K. Mesoporous Perovskite Solar Cells: Material Composition, Charge-Carrier Dynamics, and Device Characteristics. *Faraday Discuss.* **2014**, *176*, 301−312.
(37) Correa Baena, J. P.; Steier, L.; Tress, W.; Saliba, M.; Neutzner, S.; Matsui, T.; Giordano, F.; Jacobsson, T. J.; Srimath Kandada, A. R.; Zakeeruddin, S. M.; et al. Highly Efficient Planar Perovskite Solar Cells through Band Alignment Engineering. *Energy Environ. Sci.* **2015**, *8*, 2928−2934.
(38) Hovington, P.; Drouin, D.; Gauvin, R. CASINO: A New Monte Carlo Code in C Language for Electron Beam Interaction—Part I: Description of the Program. *Scanning* **1997**, *19*, 1−14.
(39) Hovington, P.; Drouin, D.; Gauvin, R.; Joy, D. C.; Evans, N. CASINO: A. New Monte Carlo Code in C Language for Electron Beam Interaction—Part III: Stopping Power at Low Energies. *Scanning* **1997**, *19*, 29−35.
(40) Drouin, D.; Couture, A.; Joly, D.; Tastet, X.; Aimez, V.; Gauvin, R. CASINO V2.42—A Fast and Easy-to-Use Modeling Tool for Scanning Electron Microscopy and Microanalysis Users. *Scanning* **2007**, *29*, 92−101.
(41) Tian, Y.; Peter, M.; Unger, E.; Abdellah, M.; Zheng, K.; Pullerits, T.; Yartsev, A.; Sundström, V.; Scheblykin, I. G. Mechanistic Insights into Perovskite Photoluminescence Enhancement: Light Curing with Oxygen Can Boost Yield Thousandfold. *Phys. Chem. Chem. Phys.* **2015**, *17*, 24978−24987.
(42) Tsai, H.; Asadpour, R.; Blancon, J.; Stoumpos, C. C.; Durand, O.; Strzalka, J. W.; Chen, B.; Verduzco, R.; Ajayan, P. M.; Tretiak, S.; et al. Light-Induced Lattice Expansion Leads to High-Efficiency Perovskite Solar Cells. *Science* **2018**, *360*, 67−70.
(43) Stranks, S. D.; Burlakov, V. M.; Leijtens, T.; Ball, J. M.; Goriely, A.; Snaith, H. J. Recombination Kinetics in Organic-Inorganic Perovskites: Excitons, Free Charge, and Subgap States. *Phys. Rev. Appl.* **2014**, *2*, No. 034007.

https://dx.doi.org/10.1021/acs.jpcc.0c06733
J. Phys. Chem. C XXXX, XXX, XXX−XXX

(44) Quitsch, W. A.; Dequilettes, D. W.; Pfingsten, O.; Schmitz, A.; Ognjanovic, S.; Jariwala, S.; Koch, S.; Winterer, M.; Ginger, D. S.; Bacher, G. The Role of Excitation Energy in Photobrightening and Photodegradation of Halide Perovskite Thin Films. *J. Phys. Chem. Lett.* **2018**, *9*, 2062−2069.
(45) Jacobsson, T. J.; Correa-Baena, J. P.; Halvani Anaraki, E.; Philippe, B.; Stranks, S. D.; Bouduban, M. E. F.; Tress, W.; Schenk, K.; Teuscher, J.; Moser, J. E.; et al. Unreacted PbI_2 as a Double-Edged Sword for Enhancing the Performance of Perovskite Solar Cells. *J. Am. Chem. Soc.* **2016**, *138*, 10331−10343.
(46) Eperon, G. E.; Stranks, S. D.; Menelaou, C.; Johnston, M. B.; Herz, L. M.; Snaith, H. J. Formamidinium Lead Trihalide: A Broadly Tunable Perovskite for Efficient Planar Heterojunction Solar Cells. *Energy Environ. Sci.* **2014**, *7*, 982−988.
(47) Saliba, M.; Matsui, T.; Seo, J.-Y.; Domanski, K.; Correa-Baena, J.-P.; Nazeeruddin, M. K.; Zakeeruddin, S. M.; Tress, W.; Abate, A.; Hagfeldt, A.; et al. Cesium-Containing Triple Cation Perovskite Solar Cells: Improved Stability, Reproducibility and High Efficiency. *Energy Environ. Sci.* **2016**, *9*, 1989−1997.
(48) Kim, D.; Jung, H. J.; Park, I. J.; Larson, B. W.; Dunfield, S. P.; Xiao, C.; Kim, J.; Tong, J.; Boonmongkolras, P.; Ji, S. G.; et al. Efficient, Stable Silicon Tandem Cells Enabled by Anion-Engineered Wide-Bandgap Perovskites. *Science* **2020**, *368*, 155−160.
(49) Christians, J. A.; Schulz, P.; Tinkham, J. S.; Schloemer, T. H.; Harvey, S. P.; Tremolet De Villers, B. J.; Sellinger, A.; Berry, J. J.; Luther, J. M. Tailored Interfaces of Unencapsulated Perovskite Solar Cells for >1,000 Hour Operational Stability. *Nat. Energy* **2018**, *3*, 68−74.
(50) Li, C.; Lu, X.; Ding, W.; Feng, L.; Gao, Y.; Guo, Z. Formability of ABX_3 (X = F, Cl, Br, I) Halide Perovskites. *Acta Crystallogr., Sect. B: Struct. Sci.* **2008**, *64*, 702−707.
(51) Nagabhushana, G. P.; Shivaramaiah, R.; Navrotsky, A. Direct Calorimetric Verification of Thermodynamic Instability of Lead Halide Hybrid Perovskites. *Proc. Natl. Acad. Sci. U.S.A.* **2016**, *113*, 7717−7721.
(52) Luo, Y. EBIC−CASINO Tool. http://fenningresearchgroup.com/wp-content/uploads/2019/06/LoadAndPlotCASINO.zip. Accessed June 17, 2019.
(53) Lee, D. S.; Yun, J. S.; Kim, J.; Soufiani, A. M.; Chen, S.; Cho, Y.; Deng, X.; Seidel, J.; Lim, S.; Huang, S.; et al. Passivation of Grain Boundaries by Phenethylammonium in Formamidinium-Methylammonium Lead Halide Perovskite Solar Cells. *ACS Energy Lett.* **2018**, *3*, 647−654.
(54) Cho, Y.; Soufiani, A. M.; Yun, J. S.; Kim, J.; Lee, D. S.; Seidel, J.; Deng, X.; Green, M. A.; Huang, S.; Ho-Baillie, A. W. Y. Mixed 3D−2D Passivation Treatment for Mixed-Cation Lead Mixed-Halide Perovskite Solar Cells for Higher Efficiency and Better Stability. *Adv. Energy Mater.* **2018**, *8*, No. 1703392.
(55) Ke, W.; Xiao, C.; Wang, C.; Saparov, B.; Duan, H. S.; Zhao, D.; Xiao, Z.; Schulz, P.; Harvey, S. P.; Liao, W.; et al. Employing Lead Thiocyanate Additive to Reduce the Hysteresis and Boost the Fill Factor of Planar Perovskite Solar Cells. *Adv. Mater.* **2016**, *28*, 5214−5221.

https://dx.doi.org/10.1021/acs.jpcc.0c06733
J. Phys. Chem. C XXXX, XXX, XXX−XXX